Fast-neutron-induced fission cross section of ^{242}Pu measured at the neutron time-of-flight facility *n*ELBE

T. Kögler,[1,2,*] A. R. Junghans,[1,*] R. Beyer,[1] M. Dietz,[1,2,†] Ch. E. Düllmann,[3,4,5] K. Eberhardt,[3,4] Ch. Lorenz,[1,2,‡] S. E. Müller,[1] R. Nolte,[6] T. P. Reinhardt,[1,2] K. Schmidt,[1,2,§] J. Runke,[3,5] R. Schwengner,[1] M. Takacs,[1,2,‖] A. Vascon,[1,3,¶] and A. Wagner[1]

[1]*Helmholtz-Zentrum Dresden - Rossendorf, 01328 Dresden, Germany*

[2]*Technische Universität Dresden, 01062 Dresden, Germany*

[3]*Institute of Nuclear Chemistry, Johannes Gutenberg University Mainz, 55099 Mainz, Germany*

[4]*Helmholtz-Institut Mainz, 55099 Mainz, Germany*

[5]*SHE Chemistry Department, GSI Helmholtzzentrum für Schwerionenforschung GmbH, 64291 Darmstadt, Germany*

[6]*Physikalisch-Technische Bundesanstalt, 38116 Braunschweig, Germany*

(Received 29 October 2018; published 1 February 2019)

The fast-neutron-induced fission cross section of ^{242}Pu was measured at the neutron time-of-flight facility *n*ELBE. A parallel-plate fission ionization chamber with novel, homogeneous, large-area ^{242}Pu deposits on Si-wafer backings was used to determine this quantity relative to the IAEA neutron cross-section standard ^{235}U(n, f) in the energy range of 0.5 to 10 MeV. The number of target nuclei was determined from the measured spontaneous fission rate of ^{242}Pu. This helps to reduce the influence of the fission fragment detection efficiency on the cross section. Neutron transport simulations performed with GEANT4, MCNP6, and FLUKA2011 are used to correct the cross-section data for neutron scattering. In the reported energy range the systematic uncertainty is below 2.7% and on average the statistical uncertainty is 4.9%. The determined results show an agreement within 0.67(16)% to recently published data and a good accordance to current evaluated data sets.

DOI: 10.1103/PhysRevC.99.024604

I. INTRODUCTION

Future nuclear power concepts with a closed fuel cycle, such as accelerator driven systems and generation IV reactors, targeted to use their fuel more efficiently, will produce less radioactive waste, meet the stringent standards of safety and proliferation resistance, and strive to be more economically competitive [1] compared to current reactor designs. Transmutation of nuclear waste in fast reactors is discussed as a way to reduce the radiotoxicity of the presently existing nuclear fuel. However, the technical realization of such plants is a challenging and expensive endeavor. Accurate nuclear data, especially fast-neutron-induced fission cross sections, are essential for new reactor designs.

^{242}Pu is the longest-lived plutonium isotope in spent nuclear fuel ($T_{1/2}$ = 375 000 yr [2]) and hence it is important for nuclear transmutation, as ^{244}Pu production is negligible [3].

Current uncertainties of the ^{242}Pu(n, f) cross section are of about 21% in the energy range from 0.5 to 2.23 MeV [4]. For a reliable prediction of the neutron multiplication and other reactor core parameters in these novel reactor concepts, the total uncertainty needs to be reduced to below 5% [4,5]. This task is addressed within the INDEN project [6], where ^{242}Pu is one of the nuclides with the highest priority.

The fast neutron-induced fission of ^{242}Pu has been studied since 1960 [7]. A brief summary of the available experimental data acquired since then has already been given in Ref. [8]. In addition, an absolute measurement of the fission cross section was also performed in Dresden in 1983 by using quasi-monoenergetic neutrons with energies of 2.6, 8.4, and 14.7 MeV [9]. Recently published measurements done at the Los Alamos National Laboratory by Tovesson *et al.* [10], at the Joint Research Center Geel by Salvador-Castiñeira *et al.* [8], and at the National Physical Laboratory of the United Kingdom in Teddington by Matei *et al.* [11] and Marini *et al.* [12] tend to be lower than present evaluated nuclear data [13]. To reduce the total uncertainty of the evaluated fission cross section, more accurate and precise nuclear data over a large energy range are needed.

This challenging task was addressed at the neutron time-of-flight (ToF) facility *n*ELBE of the Center for High-Power Radiation Sources ELBE[1] at Helmholtz-Zentrum Dresden-Rossendorf (HZDR). *n*ELBE is the first photo-neutron source

*Corresponding authors: t.koegler@hzdr.de, a.junghans@hzdr.de

†Present address: The University of Edinburgh, Edinburgh EH8 9YL, United Kingdom.

‡Present address: Lund University, P.O. Box 117, 221 00 Lund, Sweden.

§Present address: Michigan State University, 220 Trowbridge Rd East Lansing, MI 48824, USA.

‖Present address: Physikalisch-Technische Bundesanstalt, Bundesallee 100, 38116 Braunschweig, Germany.

¶Present address: ERAMET Research, 1 Avenue Albert Einstein, B.P. 120, F-78193 Trappes Cedex, France.

[1]Electron Linac for beams with high Brilliance and low Emittance.

at a superconducting electron accelerator. It allows operating the electron beam in continuous-wave (cw) mode with more than 100 kHz micropulse repetition rate. Improved neutron beam intensity, experimental conditions, e.g., a low scattering environment, and a suitable spectral fluence for fast neutron-induced reaction studies provided first-rate conditions to achieve this aim [14].

The present work reports an experiment on the neutron-induced fission cross section of ^{242}Pu relative to the IAEA neutron cross-section standard ^{235}U(n, f) [15].

II. EXPERIMENTAL SETUP

A. Fast neutrons at ELBE

The *n*ELBE photo-neutron source [16–18] produces fast neutrons with kinetic energies between 10 keV and 20 MeV. Electrons impinging on a liquid lead target produce bremsstrahlung during their deceleration. This bremsstrahlung generates the neutrons via (γ, n) reactions on the lead nuclei. The neutrons, in turn, are emitted almost isotropically from the radiator, while a large part of the electrons and the bremsstrahlung photons mainly emerge in the forward direction. To minimize the photon-to-neutron ratio, only neutrons emitted through under 100° are used in the experimental area passing a dedicated collimator system. The excellent timing of the ELBE electron beam of ∼5 ps pulse length in combination with the compactness of the neutron source, enables high resolution neutron time-of-flight experiments even at short flight paths of around 6 m.

The present experiment was performed with an electron beam energy of 30 MeV and an average bunch charge of 73 pC on the neutron-producing target. The repetition rate was 406.25 kHz. The corresponding pulse separation of 2.46 μs prevents neutron pulse overlap while still providing a beam intensity of 3.7×10^4 $n/(\mathrm{cm}^2\,\mathrm{s})$, which is sufficient for the present experiment. An absorber reducing the γ flash of the electron beam in this experiment was not required.

B. Fission chambers

A parallel-plate plutonium fission ionization chamber (hereafter PuFC) was constructed at HZDR [19,20]. It is equipped with eight large area (74 mm diameter), isotopic pure (cf. Table I), thin [96(3) to 126(4) μg/cm^2], and homogeneous deposits of ^{242}Pu, which have been produced within the TRAKULA project by Vascon *et al.* [21] at the Institute of Nuclear Chemistry of the Johannes Gutenberg University Mainz. Molecular plating was used to precipitate the fissile material from a nitrate solution on titanium coated silicon wafers of 400 μm thickness. Due to the flatness and minimal surface roughness of the Si wafers, homogeneous thin layers containing plutonium could be produced. Scanning electron microscopy with energy dispersive x-ray (SEM/EDX) measurements of the surface of the ^{242}Pu layers revealed cracks on a <1 μm scale, which are due to the drying of the isopropanol solvent used in the molecular plating. Nevertheless, the homogeneity is still better than for conventional deposition (e.g., painting or electrodeposition) on metallic foils.

TABLE I. Isotopic composition of the plutonium targets used in the PuFC and uranium targets in the H19. The tabulated values for uranium have been picked from Ref. [22]. The plutonium composition (Batch ID Pu-242-327A1) was given by the manufacturer, Oak Ridge National Laboratory (ORNL).

	Abundance (%)		
	PuFC		H19
^{238}Pu	0.0020(3)	^{234}U	0.03620(20)
^{239}Pu	0.0050(3)	^{235}U	99.9183(3)
^{240}Pu	0.0220(3)	^{236}U	0.00940(10)
^{241}Pu	0.0020(3)	^{238}U	0.03610(20)
^{242}Pu	99.9670(3)		
^{244}Pu	0.0020(3)		

The incident neutron flux of the reported experiment was determined by the well characterized ^{235}U transfer instrument H19 of PTB Braunschweig [22,23]. An overview of the key properties of the fission targets of both fission chambers is given in Table II.

Both H19 and PuFC were operated in the forward biasing mode. This means that the five double-sided fission samples of the H19 and the eight single-sided samples of the PuFC were cathodes on ground potential. Compared to the H19 electrode spacing of 5 mm, the distance between the anodes and cathodes of the PuFC was doubled, to increase the signal-to-noise ratio (charge of fission fragment induced signals compared to the charge of α-particle induced signals). The electric field strengths of the chambers, $|\vec{E}|^{\mathrm{H19}} = 240$ V cm^{-1} and $|\vec{E}|^{\mathrm{PuFC}} = 300$ V cm^{-1}, were chosen to ensure fast signals and good timing properties.

The induced charges on the anodes of the PuFC were read out by in-house developed charge-sensitive preamplifiers. Short rise times of approximately 80 ns and a signal length in the order of 400 ns reduce the pileup probability by a

TABLE II. Key parameters of the PuFC and H19 fission deposits. The areal densities and total activity of the *n*ELBE targets have been calculated from their individual spontaneous fission rates, which have been measured *in situ* and reduce the systematic uncertainties compared to conventional α spectroscopy (see Sec. II E for more details.) Their homogeneity was derived from radiographic images. The properties of the H19 fission deposits were taken from Refs. [22,23].

	PuFC (^{242}Pu)	H19 (^{235}U)
type of deposition	molecular plating	painting
no. of deposits	8 (single-sided)	5 (double-sided)
deposited area (cm^2)	43.0(5)	45.4(5)
enrichment (%)	99.9670(3)	99.9183(3)
total mass (mg)	37.24(22)	201.4(5)
areal density (μg/cm^2)	96(3)–126(4)	444(5)
total activity[a] (kBq)	8317.60	32.91
homogeneity (%)	96.7[b]	>96

[a]Including contaminants.

[b]Homogeneity means 1 minus the ratio of the standard deviation and the mean of the summed intensities of the radiographic images.

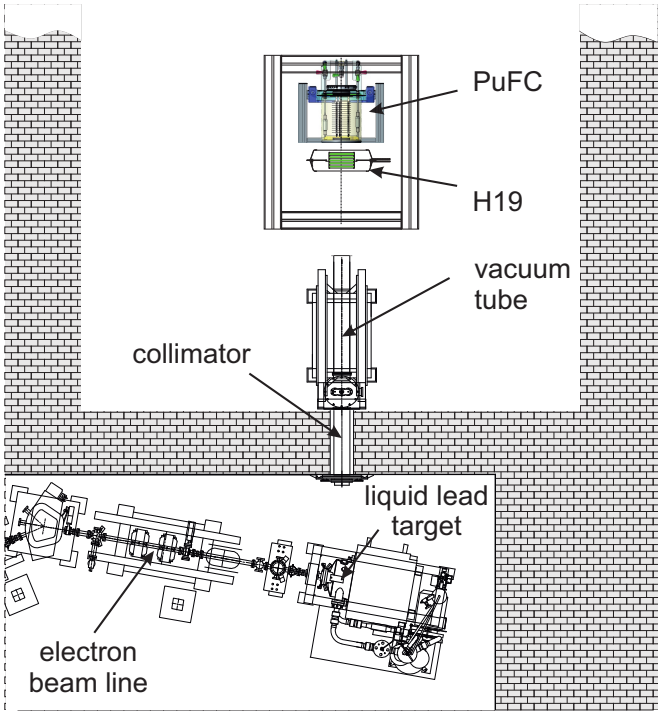

FIG. 1. Experimental setup. The ELBE electron beam comes from the lower left side and is guided to the photoneutron source. A fraction of the isotropically emitted neutrons passes a collimator and enters the low-scattering experimental area. The incident neutron flux was measured with the ^{235}U fission chamber H19. Fast neutron-induced fission events of ^{242}Pu were recorded with the fission chamber PuFC. Picture not to scale.

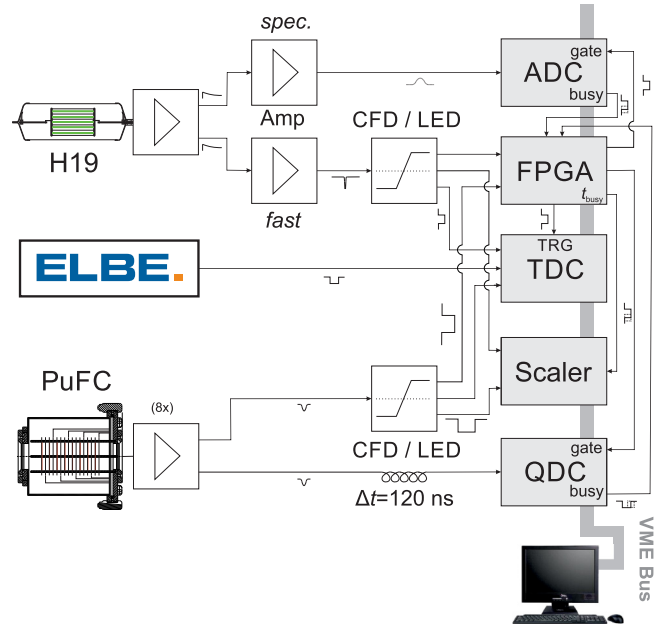

FIG. 2. Scheme of the electronic setup and the data acquisition system. The output signals of the charge-sensitive (ns) preamplifiers are split to determine the timing and the collected charge. Pulse heights of the H19 signals are acquired with an ADC after getting shaped by a spectroscopic amplifier, whereas the charge of the eight PuFC channels (only one is shown here) is determined by a QDC. The production of a fast trigger makes the use of a timing-filter amplifier in the timing branch of the H19 necessary. The second output signal is converted to a logical signal by an in-house developed discriminator (CFD/LED). The logical signals are used to determine the timing in a time-to-digital converter (TDC) and to produce a trigger for the data acquisition in an FPGA.

factor of 5 in comparison to the commonly used combination of a spectroscopic amplifier and a conventional preamplifier with μs shaping time. Further details of the *n*ELBE fission chamber can be found in Ref. [24].

C. Setup

H19 and PuFC were placed at a distance of 5.95 to 6.35 m with respect to the photoneutron source and a distance of 10 cm between each other. The neutron beam diameter in this region is between 52 and 56 mm and, therefore, always smaller than the fission targets. The beam profile was measured at different points along the neutron beam axis by using horizontally and vertically scanning plastic scintillators and was linearly interpolated to the region of interest (see Ref. [18]).

A sketch of the whole experimental setup is shown in Fig. 1. With the beam parameters chosen, the average neutron-induced fission rate of the H19 was about 31 s^{-1}. The respective photofission rate was the nearly the same. For the PuFC, the neutron-induced fission rate was 5 s^{-1}.

D. Data acquisition

The timing and energy information of both fission chambers was registered in list mode by the MBS data acquisition software developed at GSI, Darmstadt [25]. A scheme of the VME-based data acquisition electronics is shown in Fig. 2.

The signals from the ten deposits of the H19 fission chamber were summed, amplified by one charge-sensitive preamplifier, and afterwards measured by a conventional spectroscopic amplifier (Ortec 671) in the energy branch and by a timing-filter amplifier (Ortec 474) in the timing branch. The signals of the eight ^{242}Pu deposits were registered separately with the fast charge-sensitive preamplifiers mentioned in Sec. II B, to reduce possible pileup of α radioactivity of the ^{242}Pu even further.

The short signal length of the ns preamplifier allows a charge-to-digital converter (QDC, CAEN V965A) to be used. The energy deposited by the fission fragments of the H19 was determined by a peak-sensing analog-to-digital converter (ADC, CAEN V1785N).

The timing of the recorded signals was extracted by an in-house developed discriminator (CFD/LED), which combines a constant-fraction and a leading-edge discriminator. The neutron time-of-flight was measured relative to the ELBE radio frequency using a multievent/multihit time-to-digital converter (TDC, CAEN V1290A). The trigger for the whole data acquisition was a logical OR of all fission chamber channels generated by a multipurpose board (FPGA, CAEN V1495).

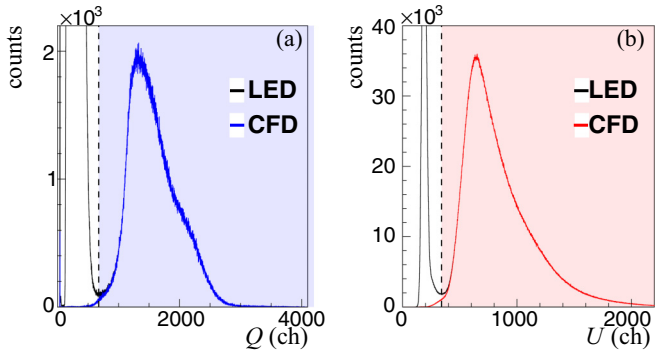

FIG. 3. Charge spectrum of channel no. 1 in the PuFC (a) and pulse height spectrum of the H19 (b). The leading-edge triggered QDC and ADC values of the chambers are shown in black, the constant-fraction triggered ones in blue or red, respectively. The colored areas indicate regions of pulse heights and charges related to fission fragments.

The leading-edge outputs of the discriminator as input for the FPGA prevents losing valid signals with slow rise time, which otherwise will not be registered due to imperfect ARC timing (**a**mplitude and **r**isetime **c**ompensated timing technique, see Ref. [26]). This was investigated to be especially important for small amplitude signals, mainly by α particles. The trigger thresholds and the delays of the CFD were chosen in such a way that the loss of fission fragments above the threshold was minimal for both chambers integrally below 0.3%. Further details of the acquisition electronics can be found in Ref. [27].

E. Analysis

The pulse-height information of the recorded list-mode data was used to separate time-independent background resulting due to the natural α decay of the target isotopes from the fission events of interest. The charge spectra show the excellent quality of the ^{242}Pu samples (cf. Fig. 3), which is expressed in a peak-to-valley ratio of 20 to 21 for all Pu deposits.

The time-of-flight spectra of each PuFC channel [e.g., channel no. 1; see Fig. 4(a)] and of the H19 [Fig. 4(c)] were calibrated with photofission events. The full width at half maximum of the photofission peak corresponds to the time resolution of the fission chambers. For the summed signal of all H19 deposits, this value is slightly higher (2.3 ns) than the single-readout PuFC value (1.7 ns).

After subtraction of a constant spontaneous fission background, the ^{242}Pu(n, f) fission rate $\dot{N}_{\mathrm{Pu},i}$ could be determined as a function of neutron kinetic energy, shown in Fig. 4(b).

A consistent energy binning for all fission targets is chosen to combine the counts of individual channels of the PuFC, which have slightly different flight paths [28]. After rebinning and background subtraction, the relative fission cross section is determined by

$$\frac{\sigma_{\mathrm{Pu}}}{\sigma_{\mathrm{U}}} = K \frac{\sum_i C_{\mathrm{Pu},i} \dot{N}_{\mathrm{Pu},i}}{\langle C_{\mathrm{U}} \rangle \dot{N}_{\mathrm{U}}} \frac{1}{I}. \quad (1)$$

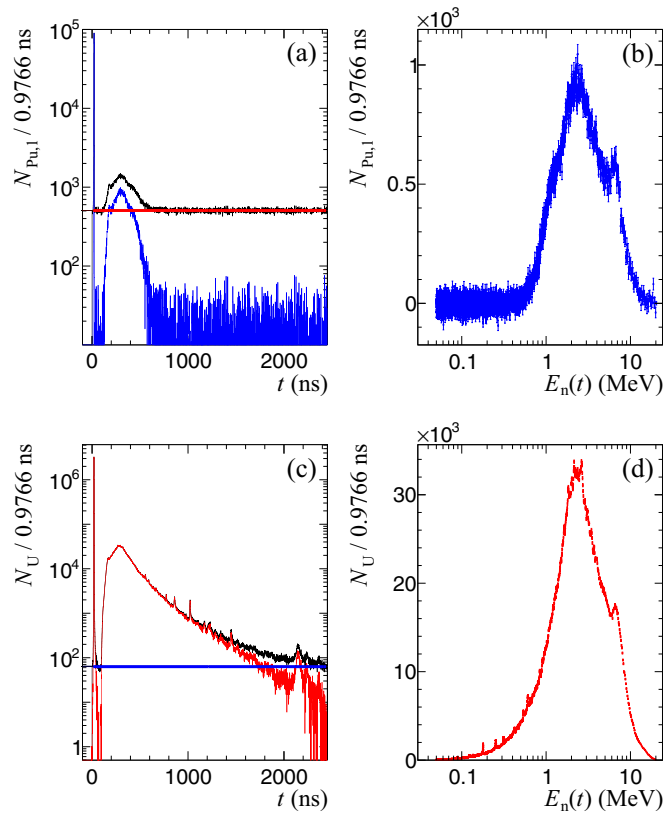

FIG. 4. Left: Detected time-of-flight spectrum N before (in black) and after (in blue for PuFC channel no. 1 and in red for H19) background subtraction. The horizontal red and blue lines indicate a constant extrapolation of the background induced by spontaneous fission events and room-return neutrons. Right: Background subtracted neutron energy distribution calculated using the time-of-flight spectrum shown on the left side.

Equation (1) is the ratio of the detected fission count rates $\dot{N}$ of both fission chambers, taking into account a neutron scattering correction C between individual fission targets for the PuFC or $\langle C_{\mathrm{U}} \rangle$ averaged over all fission layers in the case of H19. This correction factor is discussed in detail in Sec. II F. The constant factor K is the ratio of the effective total areal densities εn of both fission chambers. Here, ε is the fission fragment detection efficiency which is in general difficult to determine. For the H19, $\varepsilon_{\mathrm{U}} n_{\mathrm{U}} = 107.5(16) \times 10^{-17}$ cm^{-2} was taken from Ref. [23], whereas for the PuFC, $\varepsilon_{\mathrm{Pu}} n_{\mathrm{Pu}}$ was determined using the measured spontaneous fission rate of ^{242}Pu. This method was already introduced by Weigmann *et al.* in Ref. [29], and is feasible because the total uncertainty of the spontaneous fission partial decay constant λ_{SF} is smaller than 2% [30,31]. Taking into account the recent measurement of Salvador-Castiñeira *et al.* from Ref. [32], the weighted average (weighting according to Ref. [31]) of all available data is $\lambda_{\mathrm{SF}} = 3.25(4) \times 10^{-19}$ s^{-1}. An overview of all present data (expressed as $\ln 2/\lambda_{\mathrm{SF}}$ in units of 10^{10} yr) is given together with the evaluated values in Fig. 5.

As the area of the plutonium deposits $A_{\mathrm{Pu},i}$ is constant for all eight channels of the PuFC, the effective total areal density

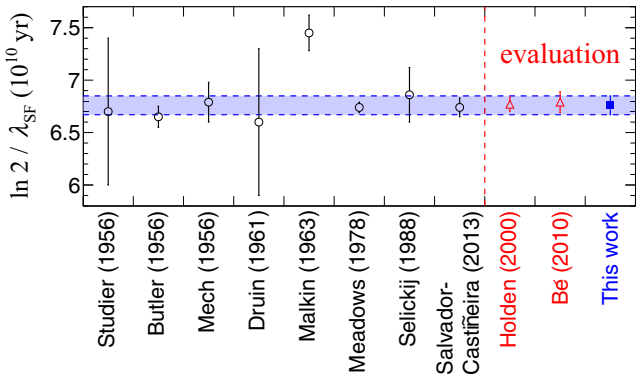

FIG. 5. Compilation of measured and evaluated partial half-lives for the spontaneous fission (SF) of ^{242}Pu. The experimental data were taken from [30,32]. The reevaluation of this data by Bé *et al.* [31] has a slightly higher uncertainty. In blue, the weighted average of all listed values is shown including the latest measurement of Salvador-Castiñeira *et al.* [32]. The blue shaded area marks the combined standard uncertainty of this value (1.3%).

$\varepsilon_{\mathrm{Pu}} n_{\mathrm{Pu}}$ is determined by

$$\varepsilon_{\mathrm{Pu}} n_{\mathrm{Pu}} = \sum_i \varepsilon_{\mathrm{Pu},i} n_{\mathrm{Pu},i} = \frac{\alpha}{A \lambda_{\mathrm{SF}}} \sum_i \dot{N}_{(\mathrm{SF}),i}. \quad (2)$$

In Eq. (2) a small dead time correction (≈1%) of the data acquisition (in the following DAQ) is introduced, denoted by α. Using this relation, the normalization factor K can be written as follows:

$$K = \frac{\varepsilon_{\mathrm{U}} n_{\mathrm{U}}}{\varepsilon_{\mathrm{Pu}} n_{\mathrm{Pu}}} = A \frac{\lambda_{\mathrm{SF}}}{\alpha} \frac{\varepsilon_{\mathrm{U}} n_{\mathrm{U}}}{\sum_i \dot{N}_{(\mathrm{SF}),i}}. \quad (3)$$

Inserting K into Eq. (1) shows that the relative cross section is independent of the fission-fragment detection efficiency of the PuFC. This only holds for small neutron energies below 10 MeV, because higher linear and angular momenta induced by the incident neutrons correspond to larger fission fragment anisotropy. This anisotropy lowers the detection efficiency. A model to calculate this effect was proposed by Carlson *et al.* in Ref. [33]. Due to the lack of experimental data for the fission fragment anisotropy and the barely known specific energy loss of fission fragments in the deposits, this inefficiency I is not an accurate value. An estimate based on the angular correlation data of Simmons *et al.* [34], a GEF2016.1.2 calculation [35] to determine the ratio of the target nuclei velocity to the average fission fragment velocity, and a GEANT4.10.1 [36] transport calculation to determine the specific energy loss of the fission fragments in the deposit is shown in Fig. 6.

F. Neutron scattering corrections

Corrections for neutron scattering are an important issue in analyzing neutron time-of-flight experiments. Two major effects play an important role: the attenuation of the neutron beam in every passed material and the loss of the correlation between neutron kinetic energy and its corresponding time-of-flight.

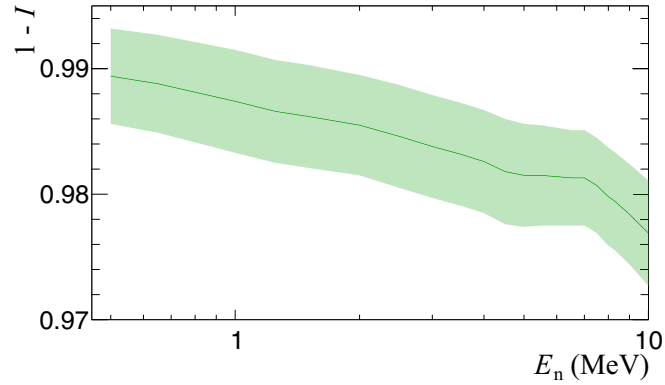

FIG. 6. Correction factor for the detection inefficiency I of fission fragments in the PuFC due to linear and angular momentum transfer according to the Carlson model [33].

The latter is important especially for inelastically scattered neutrons, because they lose a large amount of their kinetic energy within a single interaction. If such an event occurs close to a fission target, the kinetic energy of the scattered neutron determined from the measured time of flight will be much higher than the true kinetic energy, and the cross section at high neutron energies will be overestimated. Particle transport calculations allow for correcting the influence of scattering, as in these calculations both the true kinetic energy and the time of flight of the neutrons are accessible at once, which cannot be determined experimentally with the present setup. Such calculations have been performed using GEANT4.10.1 [36,37],

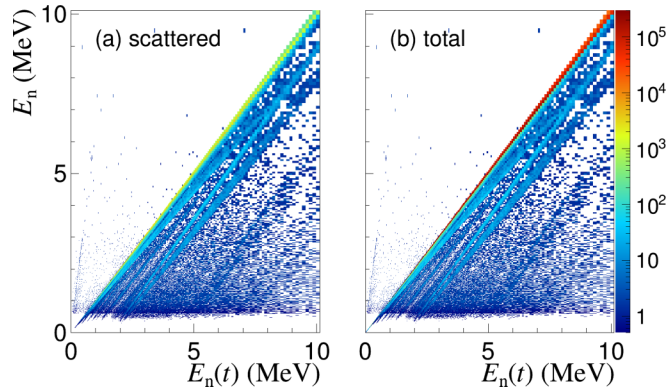

FIG. 7. Energy to time-of-flight-correlation of the last PuFC deposit in the neutron beam calculated using GEANT4.10.1. On the right-hand side (a) only events are drawn which have been scattered at least once, whereas on the left-hand side (b) all neutrons passing the actinide target are shown. The bin content of each histogram was multiplied columnwise with the ^{242}Pu fission cross section at the respective neutron energy E_n to be proportional to the fission rate. Structures off the diagonal are caused by elastic and inelastic scattering on the target backing (mostly ^{28}Si) and stainless steel windows of the fission chamber (mostly ^{56}Fe).

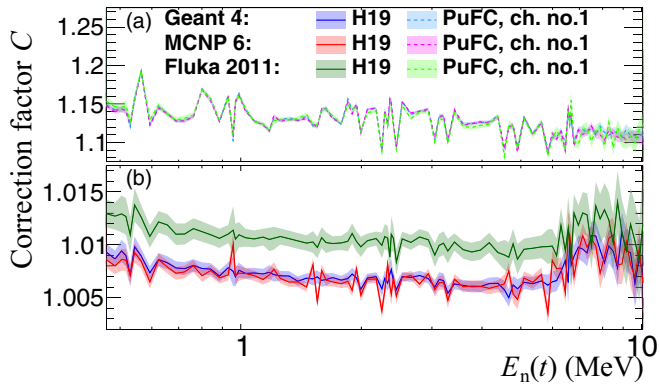

FIG. 8. Correction factor C for neutron scattering derived from GEANT4 (blue), MCNP6 (red) and FLUKA2011 (green). This plot shows the maximum effect by comparing the first target of the H19 (b) with the last target [PuFC, channel no. 1 (a)] in the neutron beam. The confidence intervals shown here as transparent ribbons correspond to the 1σ statistical uncertainty.

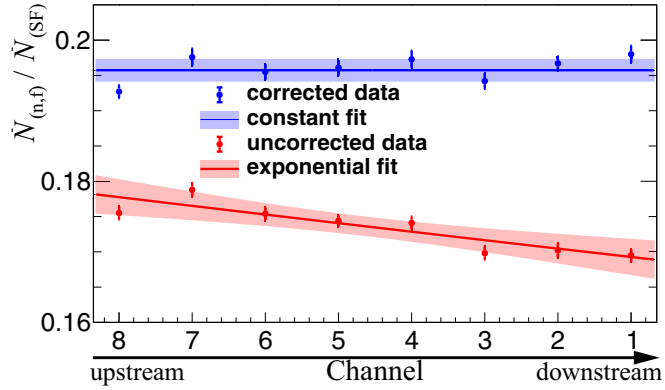

FIG. 9. Ratio of neutron-induced and spontaneous fission rate without (red) and with (blue) correction for neutron scattering. Without the correction, the fraction of the neutron-induced fission rate drops exponentially with the number of fission chamber channels, whereas the spontaneous fission rate stays constant. Note that channel no. 8 corresponds to the deposit closest to the neutron source while channel no. 1 is the farthest from it, thus having the largest absorption correction.

MCNP6.1.1 [38] and FLUKA2011 [39,40]. The geometry has been implemented identically in all three simulations, with special attention to all materials close to the neutron beam. The outcome of all event-by-event calculations is a correlation matrix of the true kinetic energy E_n and the kinetic energy $E_n(t)$ derived from neutrons' time of flight and the assumed undisturbed flight path. An example of such a correlation matrix for the last target in the beam (PuFC channel no. 1) is shown in Fig. 7.

Because scattering cross sections are energy dependent, it is necessary to use a realistic input spectrum in the simulations. The measured neutron fluence detected by the H19 was used for this purpose. The influence of neutron scattering within the H19 itself is negligible.

To correct the attenuation of the neutron beam, one can define a transmission factor

$$T_i(E_n(t)) = \frac{N_i(E_n = E_n(t))}{N_0(E_n)}, \tag{4}$$

which is the ratio of all counted neutrons N_i in the ith actinide target that have not been scattered on their way to the target (on the main diagonal on the right of Fig. 7), and the total number of neutrons N_0 that started from the neutron source. The average loss of neutrons between the first and last fission target is in the order of 15%, which is a consequence of the thickness of the Si backings and the 200 μm stainless steel windows of the PuFC.

For the loss of the energy to time-of-flight correlation, a similar correction factor k_i is defined:

$$k_i(E_n(t)) = \frac{N_i(E_n = E_n(t), E_n(t))\sigma(E_n)}{\int N_i(E_n', E_n(t))\sigma(E_n')\mathrm{d}E_n'}, \tag{5}$$

Scattered neutrons could still contribute to fission, so that k_i is the ratio of the detected fission rate of unscattered neutrons and the total detected fission rate. Because the fission rate depends on the cross section, the correlation matrices have been multiplied columnwise with the evaluated fission cross section of ^{242}Pu taken from ENDF/B-VIII.0. [41], which is for this particular reaction identical to its predecessor ENDF/B-VII.1 [13].

With Eqs. (4) and (5), the neutron scattering correction factor $C_i(E_n(t))$ is defined in the following way:

$$C_i = \frac{k_i}{T_i} \tag{6}$$

As only the sum of all H19 fission targets is available, the arithmetic mean $\langle C_U \rangle$ was calculated to take the neutron scattering within this chamber into account. The average total correction factor is in the order of 9% and is shown for all three simulations in Fig. 8. While GEANT4 and MCNP6 provide identical results within their statistical fluctuations, the FLUKA2011 results show a negligible shift towards a higher correction factor.

TABLE III. Normalization constants.

λ_{SF}	$= 3.25(4)\times10^{-19}$ s^{-1}	SF partial decay constant, cf. Fig. 5
A	$= 43.0(5)$ cm^2	actinide area, from deposition cell
ε_U	$= 0.945(14)$	fission fragment detection efficiency H19, Ref. [23]
n_U	$= 113.8(3)\times10^{17}$ cm^{-2}	atomic areal density H19, Ref. [23]
$\alpha \sum_i \varepsilon_{Pu,i}\dot{N}_{(SF),i}$	$= 29.688(4)$ s^{-1}	measured SF rate
K	$= 5.04(12)$	total normalization

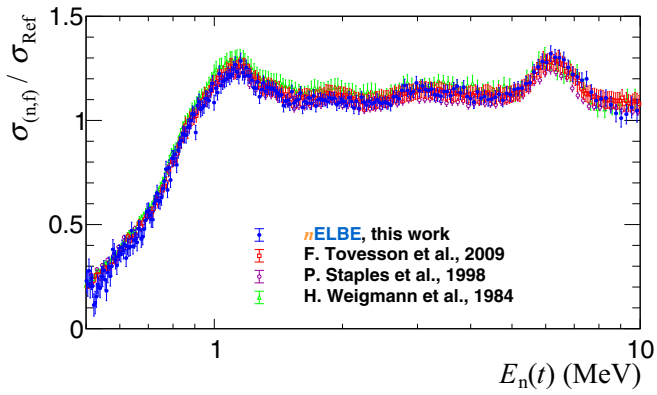

FIG. 10. Neutron-induced fission cross section of ^{242}Pu relative to the one of ^{235}U. The *n*ELBE data are shown in blue together with selected EXFOR data of Tovesson *et al.* [10], Staples *et al.* [42], and Weigmann *et al.* [29]. Within their statistical uncertainties, there is a good agreement of the presented data set with the data of Tovesson. Small deviations from the Weigmann and Staples data are clearly visible.

The correction procedure was verified by evaluating the ratio of neutron-induced and spontaneous fission rates of the PuFC. Whereas the spontaneous fission is completely independent of any scattering, the neutron-induced fission is not. The ratio shows an exponential decrease along the plutonium chamber (red line in Fig. 9) and becomes constant after applying the neutron scattering correction (blue line in Fig. 9).

III. RESULTS AND DISCUSSION

With the scattering corrections in Sec. II F and the normalization constants listed in Table. III, we are now able to calculate the relative fission cross section according to Eq. (1). The result is shown in Fig. 10 and compared to the measurements of Tovesson *et al.* [10], Staples *et al.* [42], and Weigmann *et al.* [29].

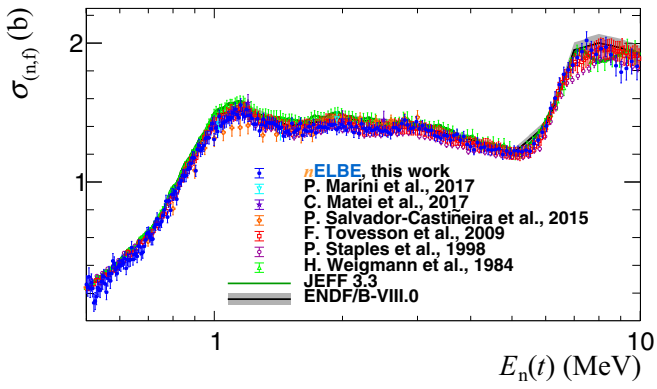

FIG. 11. Neutron-induced fission cross section of ^{242}Pu. The *n*ELBE data are shown in blue together with selected EXFOR-data of Tovesson *et al.* [10], Staples *et al.* [42], Weigmann *et al.* [29] and Salvador-Castiñeira *et al.* [8]. Within their total uncertainties, there is a good agreement of the presented data set with the data of Tovesson. Small deviations from the Weigmann data and the measurement of Salvador-Castiñeira are clearly visible.

TABLE IV. Average deviations $\Delta = \frac{\sigma^{\mathrm{EXFOR}}}{\sigma^{n\mathrm{ELBE}}} - 1$ of the measured ^{242}Pu(n, f) cross sections with respect to selected EXFOR data in the energy range of 0.5–10 MeV. The listed reduced chi square (χ^2/n) and the p value are a measure for the agreement in shape.

Measurement	*n*ELBE		
	Δ (%)	χ^2/n	p (%)
Weigmann *et al.*, 1984	3.82(16)	$229.76/161 = 1.43$	0
Staples *et al.*, 1998	−2.59(20)	$164.68/100 = 1.65$	0
Tovesson *et al.*, 2009	0.67(16)	$178.69/259 = 0.69$	100
Salvador-Castiñeira *et al.*, 2015	0.7(3)	$179.46/23 = 7.80$	0
Matei *et al.*, 2017	4.6(8)	$5.43/4 = 1.36$	25
Marini *et al.*, 2017	2(1)	$8.19/3 = 2.73$	4

Because only the relative data of Staples *et al.* were included in the EXFOR database [43], the absolute cross section of each of the other two has been divided by its reported reference cross section to fit into this plot.

To compare our measurement with other recent data sets as well, the absolute cross section was determined using the ^{235}U IAEA Neutron Cross Section Standard from Ref. [44]. This is shown in Fig. 11. All data shown in this plot were renormalized with the same standard.

One can see that there is a good overall agreement of the *n*ELBE data compared to the other selected data sets presented here. While the ratio of the *n*ELBE and the Tovesson *et al.* and Salvador-Castiñeira *et al.* data is about 0.99, larger discrepancies with the Matei *et al.* and Weigmann *et al.* data were observed especially in the plateau region between 1.2 and 5 MeV. This is of special interest, because the current European evaluation JEFF-3.3 [45] relies mainly on the latter one [29]. A comparison of shape and scale parameters of the other experimental data sets with respect to the *n*ELBE data is listed in Table IV. The average deviations with respect to ENDF/B-VIII.0 (shown in Fig. 12) are presented in Fig. 13, where the residuals of the EXFOR data are approximated by

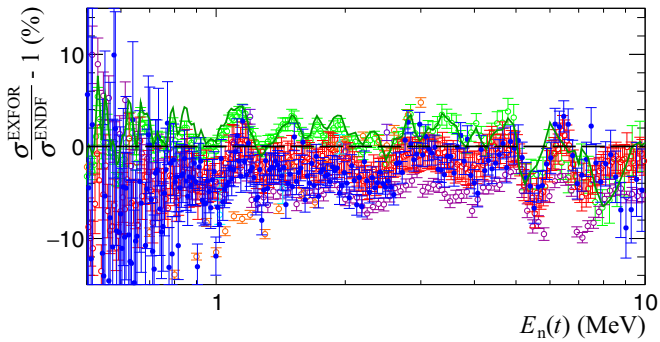

FIG. 12. Residuals of the discussed data sets shown in Fig. 11 with respect to the ENDF/B-VIII.0 evaluation. The error bars plotted here only represent the statistical uncertainty of the measurements. The used color code is identical to that in Fig. 11.

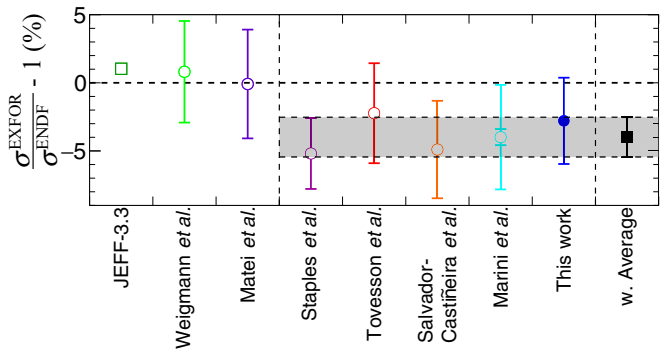

FIG. 13. Average deviations of JEFF-3.3 and selected EXFOR data sets with respect to ENDF/B-VIII.0. The weighted average has been determined by fitting a constant to the residuals shown in Fig. 12. Error bars indicating both the statistical and the total uncertainty are drawn for each data point. With the exception of the Weigmann *et al.* and Matei *et al.* data, all recent measurements tend on average to 4.1(15)% smaller cross sections compared to ENDF/B-VIII.0.

a constant. All experiments shown are on average in good agreement within their total uncertainties. The experimental data of [8,10,12,42] and this work on the average tend to be 4% lower than ENDF/B-VIII.0. In these experiments different neutron sources (spallation, photoneutron, and quasi-monoenergetic neutrons) with different reference reactions as well as different target-beam combinations were used. It seems that the systematic effects in these experiment were taken into account in a realistic way, resulting in a consistent weighted average with less than 2% uncertainty.

A. Uncertainties

Table V gives an overview of the respective contributions to the statistical and systematic uncertainties.

TABLE V. Contributions to the 1σ uncertainty of the determined cross section for neutron energies between 0.5 and 10 MeV and a time-of-flight binning of 2 ns.

Contribution	$\Delta x/x$ (%)		
	min	max	mean
Statistical			
counting statistics	1.2	47.4	4.9
scattering correction C[a]	0.17	0.93	0.21
Systematic			
normalization K			2.3
reference cross section σ_{Ref}	0.6	0.8	0.7
scattering correction C[b]	0.05	0.6	0.25
inefficiency I, cf. Fig. 6	0.38	0.43	0.41
combined			2.5

[a]The uncertainty given here only reflects the counting statistics of the simulation.
[b]From the propagated uncertainty of the underlying total cross sections.

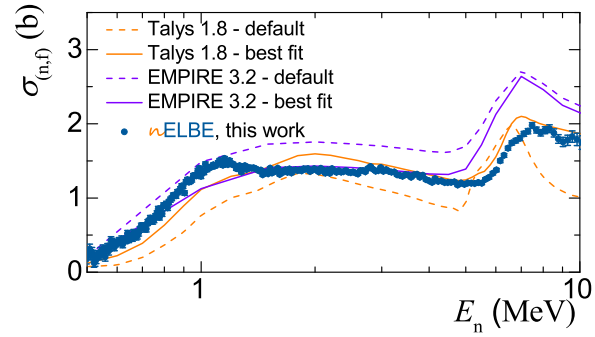

FIG. 14. Comparison of the *n*ELBE data with nuclear model calculations from TALYS1.8 and EMPIRE3.2.

For an energy range of 0.87 to 8.5 MeV the statistical uncertainty of the background-corrected counts within a 2 ns time-of-flight bin is below 3%. The highest significance is reached in the plateau region, whereas the largest uncertainties are in the threshold and second-chance fission region, where the neutron fluence of *n*ELBE is too low to achieve better statistics within the available measuring time of 80 h.

The systematic contributions from the reference cross section and the scattering corrections described in Sec. II F are always below 1% over the whole energy range. The effect of fission fragment detection inefficiency caused by the fragment anisotropy at high neutron energies (discussed in Sec. II E) increases with increasing neutron energy and is 1.6% on average for the included energy range. The largest contribution to the combined averaged systematic uncertainty of 2.9%, though, results from the uncertainty on the target area ($\sigma_A/A \approx 1.1\%$). Although radiographic images show a very homogeneous activity distribution along the whole surface (cf. Figs. 4.1.4. and 4.1.5 in Ref. [27]), the distribution at the target edges is not assessable. A conservative assumption was taken here to consider edge effects in the order of 0.4 mm with respect to the target diameter.

B. Comparison with state-of-the-art nuclear model codes

Recent nuclear model calculations show substantial deviations in comparison to all experimental neutron-induced fission cross section data of ^{242}Pu. This is exemplarily demonstrated in Fig. 14.

Here the *n*ELBE data are shown together with results from calculations performed with the nuclear model codes TALYS1.8 [46] and EMPIRE3.2 [47,48]. For both, one calculation was performed with the default settings of the code and one with an improved set of parameters. For EMPIRE, the fission barrier heights and widths have been adjusted to fit with the data. The same was also done in TALYS, but here widths, heights and additional parameters of the "Adjusted Input-Parameters" of TENDL2017 [49] were used.

The results demonstrate that nuclear fission is one of the most complex nuclear reactions and that current nuclear model codes cannot yet predict fission cross sections with the accuracy required for some technological applications.

IV. CONCLUSIONS

The fast neutron-induced fission cross section of ^{242}Pu has been measured in the range of 0.5–10 MeV at *n*ELBE. It is in good agreement to recent experimental data from different neutron facilities. The *n*ELBE data show a smaller cross section compared to recently evaluated data. In the plateau region (1.3 to 5.0 MeV), the agreement with the Staples *et al.* [$\Delta = -2.51(24)\%$, $\chi^2/n = 1.12$] and Tovesson *et al.* [$\Delta = 0.83(20)\%$, $\chi^2/n = 0.54$] data is excellent. We encountered deviations from the data of Weigmann *et al.* [$\Delta = 3.81(19)\%$, $\chi^2/n = 1.16$], which the JEFF-3.3 evaluation is mainly based on. At the plateau, where *n*ELBE has the largest neutron fluence, we achieved a statistical uncertainty of 1.1%. The systematic uncertainty is dominated by edge effects of the actinide targets and is in the order of 2.9% on average over the measured energy range.

It has been shown that neutron scattering corrections are crucial in analyzing neutron time-of-flight experiments. For the present data, the average correction was around 9%.

In comparison to state of the art nuclear model codes like TALYS1.8 and EMPIRE3.2, deviations of about 20% to 30% from all experiments are observed. This might be indicative of the predictive power of such codes on an absolute scale for neutron-induced fission cross sections of the minor actinides. Precise measurements remain the basis for nuclear data evaluation of fission cross sections.

ACKNOWLEDGMENTS

We thank Manfred Sobiella and Klaus Heidel for the support in the construction of the fission chamber and the preamplifiers. We also thank Andreas Hartmann for the continuous support in the preparation of our experiments. Thanks also go to the ELBE accelerator crew, who took care of delivering a stable and reliable beam. This work was supported by the German Federal Ministry of Education and Research under Contract No. 02NUK13A and by the European Commission within the 7th Framework Programme Fission-2013-CHANDA (Project No. 605203).

[1] The Generation IV International Forum (GIF), *Technology Roadmap Update for Generation IV Nuclear Energy Systems* (OECD-NEA, Paris, 2014).
[2] Y. Akovali, Nucl. Data Sheets **96**, 177 (2002).
[3] A. Schwenk-Ferrero, Sci. Technol. Nucl. Install. **2013**, 293792 (2013).
[4] Working Party on International Evaluation Cooperation, *Uncertainty and Target Accuracy Assessment for Innovative Systems Using Recent Covariance Data Evaluations* (OECD-NEA, Paris, 2008), http://www.oecdnea.org/science/wpec/volume26/volume26.pdf.
[5] Working Party on International Evaluation Cooperation, *The High Priority Request List for Nuclear Data (HPRL)* (OECD-NEA, Paris, 2011), http://www.oecd-nea.org/dbdata/hprl/.
[6] IAEA, *INDEN: International Nuclear Data Evaluation Network* (IAEA, Vienna, 2018), https://www-nds.iaea.org/index-meeting-crp/TM_IAEACIELO/.
[7] A. Butler, Phys. Rev. **117**, 1305 (1960).
[8] P. Salvador-Castiñeira, T. Bryś, R. Eykens, F.-J. Hambsch, A. Göök, A. Moens, S. Oberstedt, G. Sibbens, D. Vanleeuw, M. Vidali, and C. Pretel, Phys. Rev. C **92**, 044606 (2015).
[9] I. Alkhazov, E. Ganza, L. Drapchinskij, V. Dushin, S. Kovalenko, O. Kostochkin, K. Petrzhak, A. Fomichev, V. Shpakov, R. Arlt, W. Wagner, M. Josch, G. Musiol, H.-G. Ortlepp, and G. Pausch, in *Proceedings of the 3rd All-Union Conference on the Neutron Radiation Metrology at Reactors and Accelerators, Moscow* (VNIIFTRI, Moscow, 1983), Vol. 2, p. 201.
[10] F. Tovesson, T. S. Hill, M. Mocko, J. D. Baker, and C. A. McGrath, Phys. Rev. C **79**, 014613 (2009).
[11] C. Matei, F. Belloni, J. Heyse, A. J. M. Plompen, and D. J. Thomas, Phys. Rev. C **95**, 024606 (2017).
[12] P. Marini, L. Mathieu, M. Aïche, G. Belier, S. Czajkowski, Q. Ducasse, B. Jurado, G. Kessedjian, J. Matarranz, A. Plompen, P. Salvador-Castiñeira, J. Taieb, and I. Tsekhanovich, Phys. Rev. C **96**, 054604 (2017).
[13] M. Chadwick, M. Herman, P. Obložinský, M. Dunn, Y. Danon, A. Kahler, D. Smith, B. Pritychenko, G. Arbanas, R. Arcilla, R. Brewer, D. Brown, R. Capote, A. Carlson, Y. Cho, H. Derrien, K. Guber, G. Hale, S. Hoblit, S. Holloway *et al.*, Nucl. Data Sheets **112**, 2887 (2011).
[14] A. Junghans, R. Beyer, E. Grosse, R. Hannaske, T. Kögler, R. Massarczyk, R. Schwengner, and A. Wagner, Eur. Phys. J.: Web Conf. **93**, 02015 (2015).
[15] IAEA, *International Evaluation of Neutron Cross-Section Standards* (IAEA, Vienna, 2007), http://www-pub.iaea.org/MTCD/publications/PDF/Pub1291_web.pdf.
[16] E. Altstadt, C. Beckert, H. Freiesleben, V. Galindo, E. Grosse, A. Junghans, J. Klug, B. Naumann, S. Schneider, R. Schlenk, A. Wagner, and F.-P. Weiss, Ann. Nucl. Energy **34**, 36 (2007).
[17] J. Klug, E. Altstadt, C. Beckert, R. Beyer, H. Freiesleben, V. Galindo, E. Grosse, A. Junghans, D. Légrády, B. Naumann, K. Noack, G. Rusev, K. Schilling, R. Schlenk, S. Schneider, A. Wagner, and F.-P. Weiss, Nucl. Instrum. Methods A **577**, 641 (2007).
[18] R. Beyer, E. Birgersson, Z. Elekes, A. Ferrari, E. Grosse, R. Hannaske, A. Junghans, T. Kögler, R. Massarczyk, A. Matić, R. Nolte, R. Schwengner, and A. Wagner, Nucl. Instrum. Methods A **723**, 151 (2013).
[19] T. Kögler, R. Beyer, R. Hannaske, A. Junghans, R. Massarczyk, and A. Wagner, Phys. Proc. **47**, 178 (2013).
[20] T. Kögler, R. Beyer, A. R. Junghans, R. Massarczyk, R. Schwengner, and A. Wagner, Phys. Proc. **64**, 150 (2015).
[21] A. Vascon, J. Runke, N. Trautmann, B. Cremer, K. Eberhardt, and C. Düllmann, Appl. Radiat. Isot. **95**, 36 (2015).
[22] D. B. Gayther, Metrologia **27**, 221 (1990).
[23] R. Nolte, M. S. Allie, F. D. Brooks, A. Buffler, V. Dangendorf, J. P. Meulders, H. Schuhmacher, F. D. Smit, and M. Weierganz, Nucl. Sci. Eng. **156**, 197 (2007).
[24] T. Kögler, R. Beyer, K. Eberhardt, K. Heidel, A. Hartmann, A. R. Junghans, S. E. Müller, R. Nolte, M. Sobiella, A. Vascon, and A. Wagner, Nucl. Instrum. Methods A (to be published).
[25] H. G. Essel and N. Kurz, *GSI Multi-Branch System – Reference Manual*, 5th ed. (GSI, Darmstadt, 2010).
[26] Z. Cho and R. Chase, Nucl. Instrum. Methods **98**, 335 (1972).

[27] T. Kögler, Bestimmung des Neutronen-induzierten Spaltquerschnitts von ^{242}Pu, Dissertation, Technische Universität Dresden, 2016, http://nbn-resolving.de/urn:nbn:de:bsz:14-qucosa-223314.

[28] T. Kögler, R. Beyer, M. Dietz, A. R. Junghans, C. Lorenz, S. E. Müller, T. P. Reinhardt, K. Schmidt, R. Schwengner, M. P. Takacs, and A. Wagner, Eur. Phys. J.: Web Conf. **146**, 11023 (2017).

[29] H. Weigmann, J. Wartena, and C. Bürkholz, Nucl. Phys. A **438**, 333 (1985).

[30] N. E. Holden and D. C. Hoffman, Pure Appl. Chem. **72**, 1525 (2000).

[31] M.-M. Bé, V. Chisté, C. Dulieu, X. Mougeot, E. Browne, V. Chechev, N. Kuzmenko, F. Kondev, A. Luca, M. Galán, A. Nichols, A. Arinc, and X. Huang, *Table of Radionuclides*, Monographie BIPM-5, Vol. 5 (Bureau International des Poids et Mesures, Sèvres, France, 2010), http://www.bipm.org/utils/common/pdf/monographieRI/Monographie_BIPM-5_Tables_Vol5.pdf.

[32] P. Salvador-Castiñeira, T. Bryś, R. Eykens, F.-J. Hambsch, A. Moens, S. Oberstedt, G. Sibbens, D. Vanleeuw, M. Vidali, and C. Pretel, Phys. Rev. C **88**, 064611 (2013).

[33] G. W. Carlson, Nucl. Instrum. Methods **119**, 97 (1974).

[34] J. E. Simmons, R. B. Perkins, and R. L. Henkel, Phys. Rev. **137**, B809 (1965).

[35] K.-H. Schmidt, B. Jurado, and C. Amouroux, *General Description of Fission Observables – GEF Model*, JEFF Report 24 (OECD-NEA, Paris, 2014), https://www.oecd-nea.org/databank/docs/2014/db-doc2014-1.pdf.

[36] J. Allison, S. Agostinelli, K. Amako, J. Apostolakis, H. Araujo, P. Arce, M. Asai, D. Axen, S. Banerjee, G. Barrand, F. Behner, L. Bellagamba, J. Boudreau, L. Broglia, A. Brunengo, H. Burkhardt, S. Chauvie, J. Chuma, R. Chytracek, G. Cooperman *et al.*, Nucl. Instrum. Methods A **506**, 250 (2003).

[37] J. Allison, K. Amako, J. Apostolakis, P. Arce, M. Asai, T. Aso, E. Bagli, A. Bagulya, S. Banerjee, G. Barrand, B. Beck, A. Bogdanov, D. Brandt, J. Brown, H. Burkhardt, P. Canal, D. Cano-Ott, S. Chauvie, K. Cho, G. Cirrone *et al.*, Nucl. Instrum. Methods A **835**, 186 (2016).

[38] T. Goorley, *MCNP 6.1.1–Beta Release Notes* (Los Alamos National Laboratory, Los Alamos, NM, 2014).

[39] A. Ferrari, P. R. Sala, A. Fasso, and J. Ranft, *CERN 2005–10*, Vol. 10 (CERN, Geneva, 2005).

[40] T. Böhlen, F. Cerutti, M. Chin, A. Fassó, A. Ferrari, P. Ortega, A. Mairani, P. Sala, G. Smirnov, and V. Vlachoudis, Nucl. Data Sheets **120**, 211 (2014).

[41] D. Brown, M. Chadwick, R. Capote, A. Kahler, A. Trkov, M. Herman, A. Sonzogni, Y. Danon, A. Carlson, M. Dunn, D. Smith, G. Hale, G. Arbanas, R. Arcilla, C. Bates, B. Beck, B. Becker, F. Brown, R. Casperson, J. Conlin *et al.*, Nucl. Data Sheets **148**, 1 (2018).

[42] P. Staples and K. Morley, Nucl. Sci. Eng. **129**, 149 (1998).

[43] N. Otuka, E. Dupont, V. Semkova, B. Pritychenko, A. Blokhin, M. Aikawa, S. Babykina, M. Bossant, G. Chen, S. Dunaeva, R. Forrest, T. Fukahori, N. Furutachi, S. Ganesan, Z. Ge, O. Gritzay, M. Herman, S. Hlavac, K. Kato, B. Lalremruata *et al.*, Nucl. Data Sheets **120**, 272 (2014).

[44] S. Badikov, C. Zhenpeng, A. Carlson, E. Gai, G. Hale, F.-J. Hambsch, H. Hofmann, T. Kawano, N. Larson, V. Pronyaev, D. Smith, S.-Y. Oh, S. Tagesen, and H. Vonach, *International Evaluation of Neutron Cross-Section Standards*, Technical Report 07-00494 (IAEA, Vienna, 2007), http://www-pub.iaea.org/MTCD/publications/PDF/Pub1291_web.pdf.

[45] OECD and NEA, *The Joint Evaluated Fission and Fusion File (JEFF) – Version 3.3* (OECD-NEA, Paris, 2018), https://www.oecd-nea.org/dbdata/jeff/jeff33/index.html.

[46] A. Koning and D. Rochman, Nucl. Data Sheets **113**, 2841 (2012).

[47] M. Herman, R. Capote, B. Carlson, P. Obložinský, M. Sin, A. Trkov, H. Wienke, and V. Zerkin, Nucl. Data Sheets **108**, 2655 (2007).

[48] M. Sin, P. Oblozinsk, M. Herman, and R. Capote, J. Korean Phys. Soc. **59**, 1015 (2011).

[49] D. Rochman, A. J. Koning, J. C. Sublet, M. Fleming, E. Bauge, S. Hilaire, P. Romain, B. Morillon, H. Duarte, S. Goriely, S. C. van der Marck, H. Sjöstrand, S. Pomp, N. Dzysiuk, O. Cabellos, H. Ferroukhi, and A. Vasiliev, EPJ Web Conf. **146**, 02006 (2017).